Universal nonresonant absorption in carbon nanotubes

Fabien Vialla,[1] Ermin Malic,[2] Benjamin Langlois,[1] Yannick Chassagneux,[1] Carole Diederichs,[1] Emmanuelle Deleporte,[3] Philippe Roussignol,[1] Jean-Sébastien Lauret,[3] and Christophe Voisin[1,*]

[1]*Laboratoire Pierre Aigrain, École Normale Supérieure, CNRS, Université Pierre et Marie Curie, Université Paris Diderot, 24 rue Lhomond, 75005 Paris, France*

[2]*Department of Theoretical Physics, Technische Universität Berlin, Berlin, Germany*

[3]*Laboratoire Aimé Cotton, École Normale Supérieure de Cachan, Université Paris Sud, CNRS, 91405 Orsay, France*

(Received 17 July 2014; revised manuscript received 9 September 2014; published 1 October 2014)

Photoluminescence excitation measurements in semiconducting carbon nanotubes show a systematic nonresonant contribution between the well-known excitonic resonances. Using a global analysis method, we were able to delineate the contribution of each chiral species, including its tiny nonresonant component. By comparison with the recently reported excitonic absorption cross section on the S_{22} resonance, we found a universal nonresonant absorbance which turns out to be of the order of one-half of that of an equivalent graphene sheet. This value, as well as the absorption line shape in the nonresonant window, is in excellent agreement with microscopic calculations based on the density-matrix formalism. This nonresonant absorption of semiconducting nanotubes is essentially frequency independent over 0.5-eV-wide windows and reaches approximately the same value between the S_{11} and S_{22} resonances and between the S_{22} and S_{33} resonances. In addition, the nonresonant absorption cross section turns out to be the same for all the chiral species we measured in this study. From a practical point of view, this study provides a solid framework for sample content analysis based on photoluminescence studies by targeting specific excitation wavelengths that lead to almost uniform excitation of all the chiral species of a sample within a given diameter range.

DOI: 10.1103/PhysRevB.90.155401 PACS number(s): 78.67.Ch, 78.55.−m, 73.22.−f, 71.35.Cc

I. INTRODUCTION

In contrast to graphene, single-wall carbon nanotubes (SWNTs) show marked resonances in their optical spectrum that primarily reflect the one-dimensional quantum confinement of carriers. These resonances, which combine one-dimensional and excitonic characteristics, have been extensively investigated and are widely used as fingerprints of the (n,m) species [1]. However, spectroscopic studies reveal that the absorption of nanotubes does not vanish between resonances and consists of a wealth of tiny structures, such as phonon sidebands, crossed excitons (S_{ij}), or higher excitonic states [2–5]. In ensemble measurements, the nonresonant absorption is even more congested due to the contribution of residual catalyst or amorphous carbon and due to light scattering [6]. In total, a relatively smooth background showing an overall increase with photon energy is observed, from which it is challenging to extract any quantitative information.

In this study, we show that thorough photoluminescence excitation (PLE) measurements yield much finer insight into the nonresonant absorption of carbon nanotubes, which reveals the universal features of light-matter interaction in carbon nanostructures [7]. In particular, we show that the nonresonant absorption of SWNTs per unit area well above the S_{11} or S_{22} resonances reaches a universal value of 0.013 ± 0.003, in good agreement with the value $\alpha\sqrt{3}$ (where α is the fine-structure constant) predicted by a simple band-to-band theory.

*christophe.voisin@lpa.ens.fr

II. EXPERIMENTAL RESULTS

Our study of nonresonant absorption is based on a global analysis of PLE maps of ensembles of carbon nanotubes that allows us to deconvolute the contribution of each (n,m) species while keeping a high signal-to-noise ratio. The sample consists of micelle suspensions (sodium cholate) of HiPCO and CoMoCat nanotubes in deutered water (D_2O). All measurements are done at room temperature. The sample is excited by using a cw Xe lamp filtered by a monochromator that provides 5-nm-wide excitation steps throughout the near-UV, visible, and near-IR regions. The luminescence of the suspension is collected in a 90° geometry and is dispersed in a 30-cm spectrograph coupled to an InGaAs linear detector. The spectra are corrected from the grating and detector efficiencies and are normalized to the incoming photon flux. The PLE map of a HiPCo sample is displayed in Fig. 1. It consists of bright spots that correspond to the resonant S_{22} excitation of the S_{11} luminescence of the semiconducting species. The (n,m) species were identified according to the scheme developed by Bachilo *et al.* [1]. These spots are surrounded by a weak but nonvanishing background that shows up as vertical light-blue strips in the map. In contrast to absorption measurements, the presence of such a background in a luminescence measurement shows that there is actual absorption by the very species that give rise to the IR luminescence, that is, the semiconducting nanotubes themselves. Due to the luminescence detection scheme, this background can be unambiguously distinguished from contributions such as elastic light scattering, absorption by metallic species or by catalyst, or amorphous carbon particles that blur the nonresonant response of the sample in linear absorption measurements.

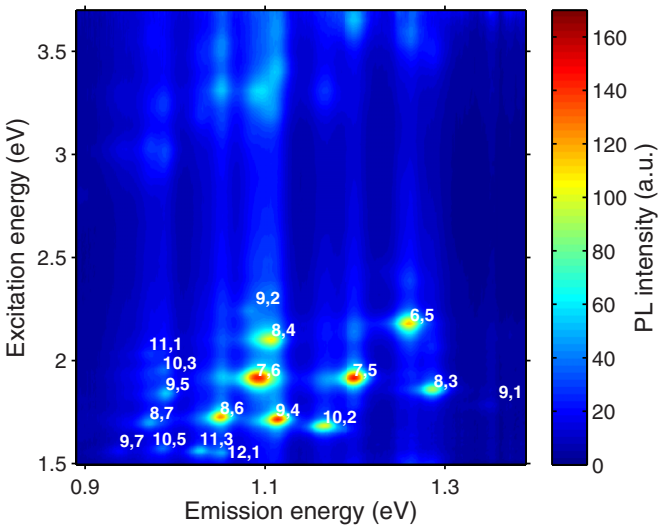

FIG. 1. (Color online) Photoluminescence map of a micelle suspension of HiPCO nanotubes in D_2O. The (n,m) indices are assigned to each PL resonance according to the scheme of Ref. [1]. The spots at the bottom of the map correspond to the excitation on the S_{22} resonances of the nanotubes, whereas the spots in the upper part of the map correspond to the excitation on the S_{33} levels.

This point is illustrated in Fig. 2, where the linear absorption spectrum of a (6,5) chirality-enriched sample (NanoIntegris) is compared to the PLE spectrum of the same sample. Both spectra are normalized to the maximum of the S_{22} resonance in order to compare their background levels. The latter appears to be 2 to 3 times lower in the case of the PLE spectrum, showing that extrinsic contributions in the linear absorption spectrum are sizable even for sorted samples.

Importantly, PLE and absorption spectra can be directly compared if the relaxation from the upper levels down to the light-emitting level is much faster than the competing relaxation processes [8]. Several time-resolved studies have shown that nonresonant excitation of SWNTs leads to extremely fast (subpicosecond) relaxation to the lower bright level [9–11]. We also checked with two-color pump-probe measurements that the population buildup time on the S_{11} level does not depend on the pump wavelength (see the Appendix, Fig. 7). To further make sure that this internal conversion is faster than the competing relaxation processes, we varied the latter by changing the temperature of the sample (from 10 to 300 K) [12] and checked that the PLE spectrum remained unchanged (see the Appendix, Fig. 8). In total, we can safely assume that nonresonant PLE measurements accurately reflect the absorption properties of SWNTs.

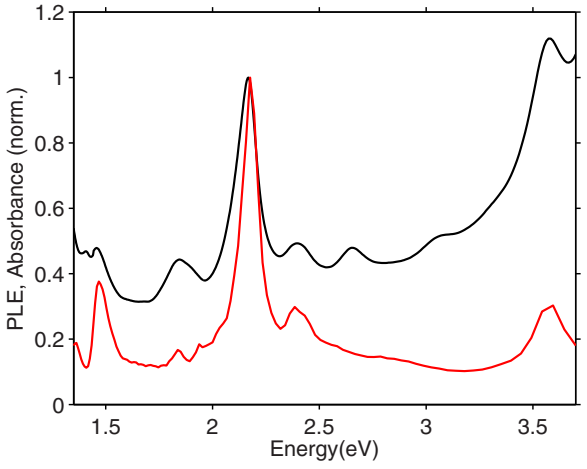

FIG. 2. (Color online) Linear absorption spectrum (black) and PLE spectrum (red) of a (6,5) enriched suspension. Both spectra are normalized to the maximum of the S_{22} resonance to show their respective background contributions.

Due to the numerous chiral species present in the sample and due to the partial spectral overlap of their IR emission lines, a specific analysis method is required in order to quantitatively assess the nonresonant absorption of each species. To this end, we developed a global fitting procedure: When the luminescence is excited at the S_{22} resonance of a given (n,m) species, the corresponding S_{11} emission line becomes the dominant feature of the luminescence spectrum, thus making it possible to determine accurately the emission energy and the width. We performed such a preliminary fitting for each (n,m) species emission line. From this set of S_{11} energies and widths, we constructed a model function made of the sum of Lorentzian profiles with free amplitudes and fixed energies and widths. Finally, the PL spectrum obtained for each excitation wavelength was fitted to the model function (see the Appendix, Fig. 10). The resulting amplitude of each Lorentzian component defines the PLE amplitude of the corresponding (n,m) species at this excitation wavelength [13].

Such a deconvoluted PLE spectrum is displayed in Fig. 3 for two exemplary species. The most prominent features are the S_{ii} resonances (essentially, the S_{22} and S_{33} ones) and the associated phonon sidebands [2,3]. An additional weaker resonance is observable roughly 0.5 eV above the S_{22} resonance that might be attributed to the S_{23} cross-polarized transition [4]. In addition to these features, a background is obtained between the excitonic resonances in the PLE measurements. This background is readily observable as a plateau in the 0.5-eV-wide energy window free of any resonant feature on the red side of each excitonic resonance. It represents roughly 15% of the S_{22} absorption cross section. Interestingly, we can compare the deconvoluted PLE spectrum of a given species [namely, the (6,5) one] for two types of samples [black (for HiPCO) and red (for CoMoCat) lines in Fig. 3(a)]. Although these samples differ in both the growth method and the postgrowth processing, the PLE spectra are remarkably similar, confirming that the nonresonant signal has an intrinsic origin.

In order to be more quantitative, we make use of our recent measurement of the absolute value of the S_{22} absorption cross section of most of the chiral species present in this sample [14] to rescale the PLE axis into the absorption cross section. In order to take into account the total number of carbon atoms involved in the absorption for each species, we further calculate the (unitless) absorption cross section per unit area by dividing the absorption cross section by πd_t, where d_t is the tube diameter. In addition, this approach provides a direct comparison with the case of graphene, which shows a frequency-independent absorption cross section of $\pi\alpha = 0.023$ in the visible and near-IR regions [7].

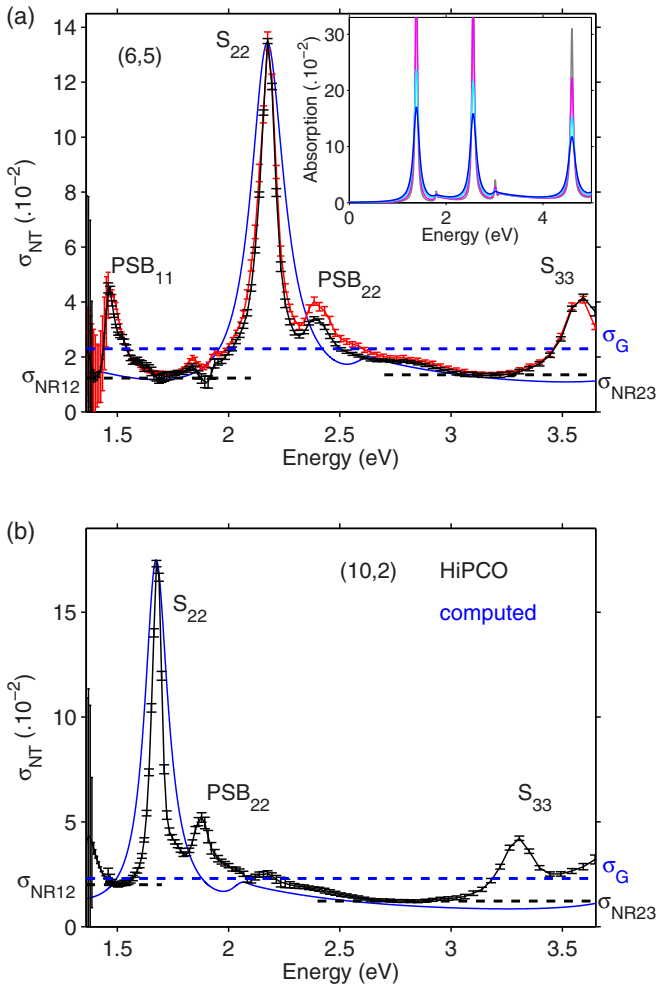

FIG. 3. (Color online) Deconvoluted PLE spectra for the (a) (6,5) and (b) (10,2) species [HiPCO (black) and CoMoCat (red)] extracted from the PL map of Fig. 1. The absolute value of σ is retrieved from the knowledge of the resonant S_{22} absorption cross section [14] and assuming a flat internal conversion rate. The values are expressed per unit area, allowing a direct comparison with the graphene case. The blue dashed line represents the equivalent absorption of a graphene layer. The black dashed lines show the nonresonant absorption plateaus that make up the input of Fig. 5. The solid blue line is the microscopic calculation of the absorption spectrum of the corresponding species after applying a global energy shift and a global convolution with a (a) 150 meV or (b) 130 meV broad Lorentzian. The inset in (a) shows the calculated spectra for a set of broadenings of 70, 100, 150, and 200 meV, showing that the magnitude and the shape of the nonresonant absorption are hardly altered.

The nonresonant contribution of SWNTs is defined as the minimum of the absorption cross section between two resonances, which practically corresponds to a 500-meV-wide plateau on the red side of each S_{ii} resonance. We note that depending on the chiral species, trigonal warping effects can spread the transition energies, leading to wider observation windows for the nonresonant signal (between the S_{22} and S_{33} transitions for type II species, for instance). Conversely, for large-diameter nanotubes, the limited energy splitting between resonances (which may become comparable to their width) may compromise the observation of the plateau or warp its value.

The observation of this nonresonant background is consistent with former PLE measurements [5,15] and with recent absorption studies conducted for individual large-diameter nanotubes between higher transitions [16,17] that systematically show a sizable background between higher transitions. These studies are in agreement with our observations regarding both the profile and the magnitude of the nonresonant signal.

III. THEORETICAL MODELING

We were able to quantitatively reproduce this nonresonant absorption spectrum within microscopic calculations based on the density-matrix formalism combined with tight-binding wave functions [18]. The calculation of the frequency-dependent absorption coefficient $\alpha(\omega)$ requires knowledge of the microscopic polarization $p_k(t) = \langle a^+_{vk} a_{ck} \rangle$, which is a measure of the transition probability between the conduction and the valence bands at wave vector k [18]. Applying the Heisenberg equation of motion and exploiting the fundamental commutator relations, we obtain the corresponding semiconductor Bloch equation for $p_k(t)$ within the limit of linear optics [18]:

$$\dot{p}_k(t) = -i\,\Delta\tilde{\omega}_k\, p_k(t) + i\,\tilde{\Omega}_k(t) - \gamma\, p_k(t). \tag{1}$$

The dephasing of the microscopic polarization is taken into account by the parameter γ, which determines the linewidth of optical transitions. The Coulomb interaction is considered within the screened Hartree-Fock level and leads to a renormalization of the transition energy $\Delta\varepsilon_k = \hbar[\omega_c(k) - \omega_v(k)]$ due to the repulsive electron-electron interaction $W_{e-e}(k,k')$,

$$\hbar\Delta\tilde{\omega}_k = \Delta\varepsilon_k - \sum_{k'} W_{e-e}(k,k'), \tag{2}$$

and to the renormalization of the Rabi frequency $\Omega_k(t) = i\,\frac{e_0}{m_0} M_z^{cv}(k) A_z(t)$ due to the attractive electron-hole interaction $W_{e-h}(k,k')$,

$$\tilde{\Omega}_k(t) = \Omega_k(t) + \frac{1}{\hbar}\sum_{k'} W_{e-h}(k,k')\, p_{k'}(t)\,. \tag{3}$$

Here, $M_z^{cv}(k)$ is the optical matrix element describing the strength of the carrier-light coupling, and $A_z(t)$ is the vector potential denoting the optical excitation of the system with light polarized along the nanotube axis (here, the z axis). We obtain an analytic expression for $M_z^{cv}(k)$ within the nearest-neighbor tight-binding approximation [19]. The screened Coulomb matrix elements $W^{vk',vk}_{vk,vk'}$ determining $W_{e-e}(k,k')$ and $W^{vk',vk}_{vk,vk'}$ in Eqs. (2) and (3) [20] are obtained by explicitly calculating the appearing tight-binding coefficients and by applying the Ohno parametrization of the Coulomb potential, which is known to be a good approximation for carbon nanotubes [21].

By numerically evaluating the Bloch equation for the microscopic polarization $p_k(t)$, we have access to the absorption of carbon nanotubes with an arbitrary chiral angle and with a wide range of diameters. Here, we calculated the absorption coefficient of the investigated (6,5) and (10,2) nanotubes representing near-armchair and near-zigzag species

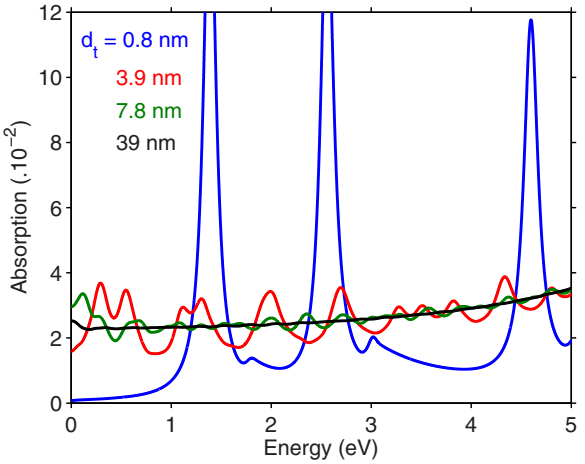

FIG. 4. (Color online) Calculated absorption of nanotubes for selected diameters. For larger diameters, the absorption clearly becomes diameter independent and reaches that of graphene. The calculations are normalized to set the value of this plateau to $\pi\alpha$.

(Fig. 3). The absolute value of the absorption was obtained by scaling the graphene absorption calculated in the same way as $\pi\alpha$ [7,22]. We further checked that the calculated absorption of very large nanotubes tends to the graphene limit (Fig. 4). In order to match the experimentally measured S_{22} resonance, we applied a global energy shift to the theoretical spectra to account for the environment-induced screening of the Coulomb potential [23] and a broadening of $\simeq$150 meV to account for the many-particle-induced broadening that has not been considered on the applied Hartree-Fock level. Note that the broadening does not alter the nonresonant absorption value since the variations of the latter are very small at this scale (see inset in Fig. 3). The agreement between theory and experiment is remarkable regarding this nonresonant absorption in the sense that there are no free parameters in the theory. In particular, both the amplitude and the profile of the nonresonant spectrum are very well reproduced. In contrast, the excitonic resonances significantly differ, which can probably be traced back to the presence of phonon-induced and other sidebands that have not been taken into account in the theory and that withdraw parts of the oscillator strength from the main excitonic transition.

IV. DISCUSSION

The experimental nonresonant absorption contribution was extracted for ten species (Fig. 5). This absorption shows no clear dependence on the diameter of the species, with overall variations being smaller than the mean error bar. We also examined a possible dependence on the chiral angle but could not see any effect (see the Appendix, Fig. 11). This is in strong contrast to the case of the resonant S_{22} transition, which shows a remarkable chiral angle dependence [14,24]. Notably, the nonresonant absorption cross section is almost identical between the S_{11} and S_{22} resonances and between the S_{22} and S_{33} resonances and corresponds to approximately one-half of the value for graphene.

Interestingly, most of these observations, including the nonresonant absorption of approximately one–half of that of

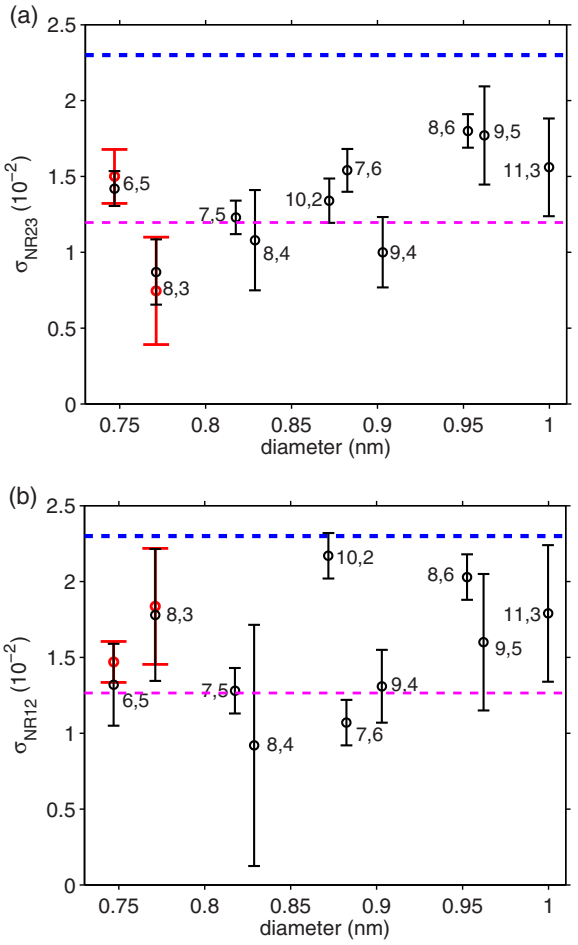

FIG. 5. (Color online) Diameter dependence of the nonresonant absorption contribution extracted from deconvoluted PLE spectra for ten species (a) between the S_{22} and S_{33} (σ_{NR23}) transition and (b) between the S_{11} and S_{22} transition (σ_{NR12}). The black symbols stand for the HiPCO material, and the red ones are for the CoMoCat material. The blue dashed line represents the graphene absorption, while the magenta dashed line shows nonresonant absorption of nanotubes estimated within the zone-folding approximation.

graphene, can be qualitatively understood in the framework of a simple band-to-band absorption theory. Actually, the nonresonant contribution is observed for energies well above the excitonic resonance, where Coulomb correlation corrections are expected to be weak. In fact, this independent electron description provided an accurate computation of the graphene absorption in the near-IR and visible ranges [7,25]. Let us first note that from a simple oscillator-strength-conservation argument, the background absorption of nanotubes is expected to be smaller than that of graphene because most of the oscillator strength is transferred into the resonances of the nanotubes. More quantitatively, the absorption probability is given by Fermi's golden rule and involves the dipolar matrix elements and the joint density of states (JDOS) between the valence and conduction subbands. In a first approximation, the latter can be obtained from a zone-folding approach using the conical approximation for the graphene band structure in the vicinity of the K points. The JDOS of a nanotube is computed per graphene unit cell (or, equivalently, per two

carbon atoms) [26]:

$$j_{NT}(\omega) = \frac{\sqrt{3}a^2}{2\pi^2 \hbar v_F d_t} \sum_i g(\hbar\omega, S_{ii}), \quad (4)$$

where

$$g(\hbar\omega, E_i) = \begin{cases} \hbar\omega / \sqrt{(\hbar\omega)^2 - E_i^2} & \text{if } \hbar\omega > E_i, \\ 0 & \text{if } \hbar\omega < E_i, \end{cases}$$

where a is the length of the graphene lattice base vector, $v_F = 10^6\ \mathrm{m\,s^{-1}}$ is the graphene Fermi velocity, and d_t is the nanotube diameter. Using the same notations, the joint density of states per unit cell for graphene reads

$$j_G(\omega) = \frac{\sqrt{3}a^2}{8\pi(\hbar v_F)^2}\hbar\omega. \quad (5)$$

The key point here is that $j_{NT}(\omega)$ tends to a plateau when the photon energy is much larger than the band-edge energy and increases stepwise for each additional S_{ii} transition. This is in contrast to the case of graphene, where the joint density of states grows linearly with the photon energy, leading to the well-known frequency-independent absorption probability. The link between the two-dimensional graphene case and its one-dimensional carbon nanotube counterpart lies in the number of plateaus that fit within the $\hbar\omega$ energy window. Therefore, there is a profound relationship between the absorption probability of a nanotube away from the resonances and that of a graphene layer.

In a first approximation, we neglected the possible variations of the matrix element with the direction of electron wave vector. Due to the overall frequency dependence of the optical matrix element and of the prefactors [19,27], the JDOS plateaus turn into slowly decreasing tails in the absorption spectrum (Fig. 9), in agreement with the experimental observations and the microscopic calculations (see Fig. 3).

More quantitatively, this simple model allows us to compare the JDOS per carbon atom (and therefore the absorption) in the cases of graphene and of nanotubes at a photon energy at the foot of the S_{ii} resonances of the nanotubes (where the nonresonant contribution is most readily observable; Fig. 3). One finds $j_{NT}/j_G = \sqrt{3}/\pi \simeq 0.55$ at the foot of the S_{22} transition and $j_{NT}/j_G = \frac{3}{4\pi}(\frac{4}{\sqrt{15}} + \frac{2}{\sqrt{3}}) \simeq 0.52$ at the foot of the S_{33} transition, leading to an absorption of $\simeq$0.012 in the nanotube case, in good agreement with the mean experimental value 0.013 ± 0.003 (Fig. 5).

Incidentally, this universal nonresonant absorption (which does not depend on the frequency, the transition order, nor the chiral species) explains why nonresonantly excited photoluminescence spectra are empirically known to give a good image of the chiral species content of a sample. This effect simply results from the fact that such a nonresonant excitation provides a uniform excitation of the sample at a given wavelength regardless of the chiral species. This effect is depicted in Fig. 6, where the linear absorption spectrum of a HiPCO sample is compared to its PL spectrum excited off resonance (for a laser wavelength falling in between the S_{22} and S_{33} resonances of most chiral species). It is clearly observable that the magnitude of the lines observed in the PL spectrum is in good agreement with that of the absorption spectrum.

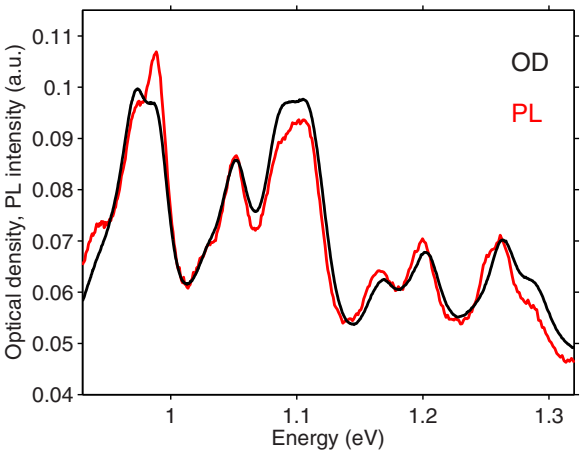

FIG. 6. (Color online) Absorption spectrum (black line) of a sodium cholate suspension of HiPCO nanotubes (offset corrected). PL spectrum (red line) of the same sample for an off-excitation wavelength at 3 eV.

In conclusion, we used PLE measurements with a global fitting analysis to delineate the contribution of each (n,m) species to the nonresonant absorption background of a micelle suspension of SWNTs. We showed that this nonresonant absorption reaches a universal value for all chiral species that is equal to approximately one-half of the value of the unrolled graphene sheet both between the S_{11} and S_{22} resonances and between the S_{22} and S_{33} resonances. In addition, this nonresonant absorption hardly depends on the photon energy over 0.5-eV-wide windows between excitonic resonances. These properties of the nonresonant absorption of SWNTs were quantitatively reproduced by microscopic calculations based on the density-matrix formalism. This study has practical implications for unconventional excitation schemes of ensembles of SWNTs. Furthermore, it exemplifies the profound link between the photophysical properties of the different nanocarbons.

ACKNOWLEDGMENTS

This work was supported by the GDR-I GNT and the ANR grant "TRANCHANT." C.V. is a member of Institut Universitaire de France. E.M. acknowledges financial support from the Einstein Foundation Berlin.

APPENDIX

1. Time-resolved measurements

Femtosecond pump-probe measurements were carried out to probe the population buildup dynamics of the S_{11} level subsequent to either S_{22} or nonresonant excitation (Fig. 7). The strictly identical rise times of the transients (within our 250-fs time resolution) are consistent with ultrafast internal conversion, making a direct scaling of PLE spectra into absorption possible.

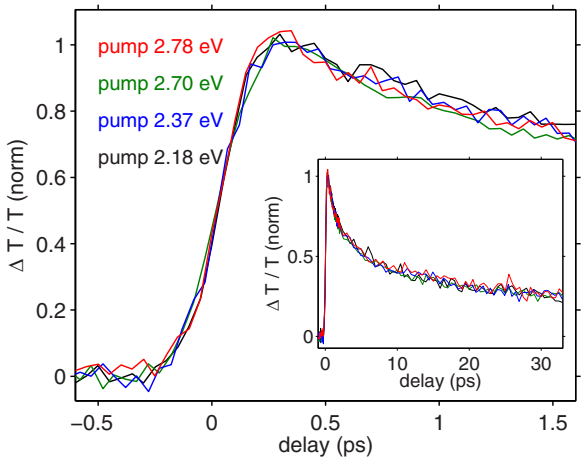

FIG. 7. (Color online) Transient bleaching of the S_{11} transition of (6,5) nanotubes in a micellar suspension subsequent to femtosecond excitation either at their S_{22} transition (black line) or at several nonresonant energies indicated in the legend. In all cases, the product of the pump-power density and the absorbance was kept constant, resulting in similar excitation densities. The inset shows the same data plotted on an extended time window.

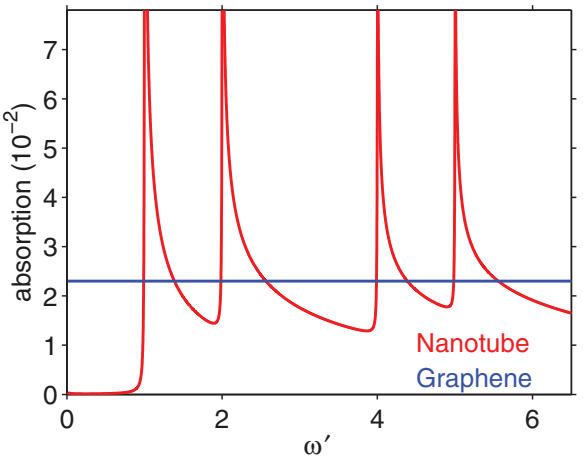

FIG. 9. (Color online) Absorption calculated from the joint density of states in the conical zone-folding approximation (red line) as a function of the reduced energy $\omega' = 3\omega d_t/(4v_F)$, where $v_F \simeq 1 \times 10^6$ m s^{-1} stands for the graphene Fermi velocity. The amplitude is rescaled globally so that the value computed for a graphene layer matches the universal value of 0.023 (blue solid line). An effective broadening of 0.01 eV was used.

2. Temperature dependence

We measured the PLE spectrum (Fig. 8) of an ensemble of nanotubes deposited on a quartz plate as a function of temperature. After normalization, the PLE profiles are identical, showing that the internal relaxation towards the S_{11} level is much faster than any other competing process. In fact, if this were not the case, the temperature-induced changes expected for these processes would warp the PLE profile.

3. Band-to-band calculations

Figure 9 shows the absorption spectrum calculated in the band-to-band approximation both for graphene and nanotubes as a function of reduced frequency $\omega' = 3\omega d_t/(4v_F)$, where $v_F \simeq 1 \times 10^6$ m s^{-1} stands for the graphene Fermi velocity. The JDOS plateaus of the nanotube give rise to slowly decreasing absorption tails between the resonances, reaching approximately one-half of the absorption of graphene at the foot of each resonance.

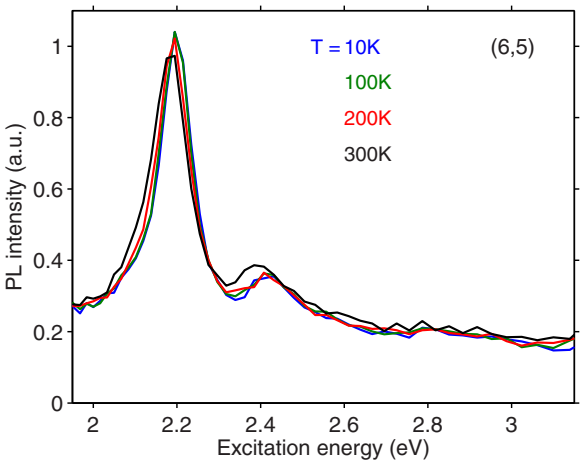

FIG. 8. (Color online) Normalized PLE spectra of the (6,5) species measured at several temperatures.

4. Global analysis method

The efficiency of the global analysis method is exemplified in Fig. 10, where the contributions of minority species showing up as side peaks in regular PLE spectra are efficiently suppressed in the deconvoluted PLE spectrum.

5. Chiral angle dependence

The nonresonant absorption cross section extracted for ten chiral species can be plotted as a function of their chiral angle (Fig. 11). Following previous studies [14], we instead plot them as a function of the trigonal parameter $q \cos 3\theta$ (where $q = n - m$ mod 3), which is more suited to describing chiral variations of the electronic properties in SWNTs. Within our error bars, we do not observe any systematic variation of the nonresonant absorption with the chiral angle. However, a nascent trend can be guessed that would correspond to a decrease of σ_{NR12} with increasing $q \cos 3\theta$ and a symmetrical increase of σ_{NR23}. We believe that these are not intrinsic features but that this rather arises from the decrease with increasing $q \cos 3\theta$ of the energy splitting between the S_{22} and S_{33} resonances as a consequence of the trigonal warping (and inversely for S_{11} and S_{22}). Therefore, the background is slightly overestimated for σ_{NR23} due to overlapping with the tails of the resonances for positive $q \cos 3\theta$ values (and the inverse for σ_{NR12}).

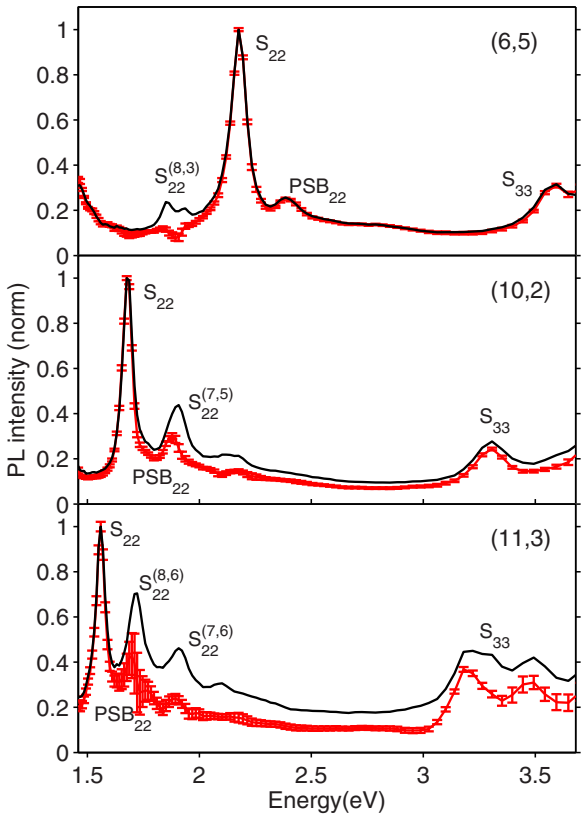

FIG. 10. (Color online) Comparison of regular PLE spectra (black solid line) with deconvoluted spectra (red line) from the global analysis method for selected chiral species with associated error bars.

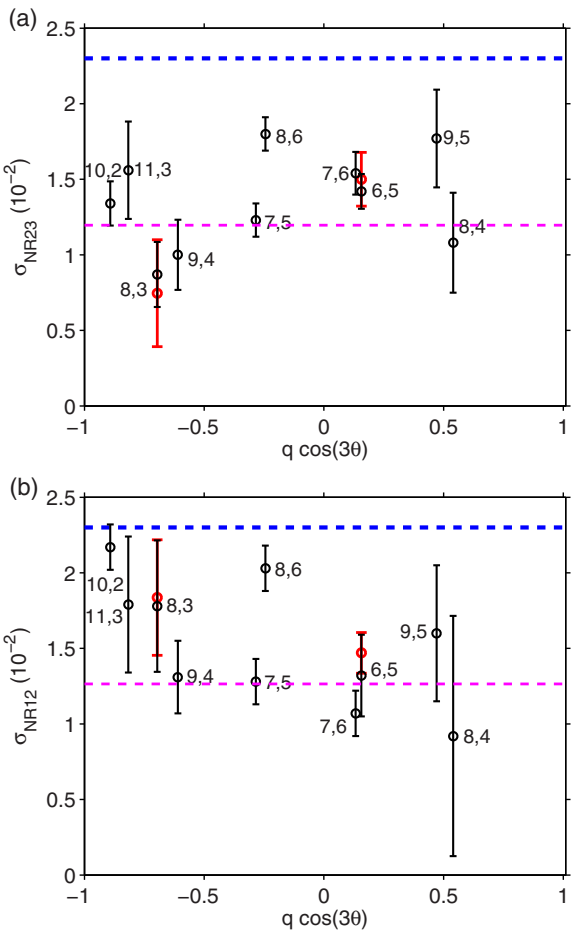

FIG. 11. (Color online) Nonresonant absorption of several chiral species measured at the foot of their (a) S_{33} and (b) S_{22} transitions as a function of the trigonal parameter $q \cos 3\theta$, where $q = n - m$ mod 3.

[1] S. M. Bachilo, M. S. Strano, C. Kittrell, R. H. Hauge, R. E. Smalley, and R. B. Weisman, Science **298**, 2361 (2002).

[2] F. Plentz, H. B. Ribeiro, A. Jorio, M. S. Strano, and M. A. Pimenta, Phys. Rev. Lett. **95**, 247401 (2005).

[3] S. Berciaud, C. Voisin, H. Yan, B. Chandra, R. Caldwell, Y. Shan, L. E. Brus, J. Hone, and T. F. Heinz, Phys. Rev. B **81**, 041414 (2010).

[4] Y. Miyauchi, M. Oba, and S. Maruyama, Phys. Rev. B **74**, 205440 (2006).

[5] J. Lefebvre and P. Finnie, Nano Lett. **8**, 1890 (2008).

[6] A. V. Naumov, S. Ghosh, D. A. Tsyboulski, S. M. Bachilo, and R. B. Weisman, ACS Nano **5**, 1639 (2011).

[7] R. R. Nair, P. Blake, A. N. Grigorenko, K. S. Novoselov, T. J. Booth, T. Stauber, N. M. R. Peres, and A. K. Geim, Science **320**, 1308 (2008).

[8] G. Bastard, *Wave Mechanics Applied to Semiconductor Heterostructures* (Wiley, New York, 1988), Chap. 7, Sec. III.

[9] J. S. Lauret, C. Voisin, G. Cassabois, C. Delalande, P. Roussignol, L. Capes, and O. Jost, Phys. E (Amsterdam, Neth.) **17**, 380 (2003).

[10] C. Manzoni, A. Gambetta, E. Menna, M. Meneghetti, G. Lanzani, and G. Cerullo, Phys. Rev. Lett. **94**, 207401 (2005).

[11] C. Köhler, T. Watermann, and E. Malic, J. Phys. Condens. Matter **25**, 105301 (2013).

[12] S. Berger, C. Voisin, G. Cassabois, C. Delalande, P. Roussignol, and X. Marie, Nano Lett. **7**, 398 (2007).

[13] Note, however, that this method is not applicable for the species whose emission energy difference is much smaller than their emission linewidth, giving completely overlapping contributions.

[14] F. Vialla, C. Roquelet, B. Langlois, G. Delport, S. M. Santos, E. Deleporte, P. Roussignol, C. Delalande, C. Voisin, and J.-S. Lauret, Phys. Rev. Lett. **111**, 137402 (2013).

[15] Y. Kimoto, M. Okano, and Y. Kanemitsu, Phys. Rev. B **87**, 195416 (2013).

[16] J.-C. Blancon, M. Paillet, H. N. Tran, X. T. Than, S. A. Guebrou, A. Ayari, A. S. Miguel, N.-M. Phan, A.-A. Zahab, J.-L. Sauvajol, N. D. Fatti, and F. Vallée, Nat. Commun. **4**, 2542 (2013).

[17] K. Liu, X. Hong, S. Choi, C. Jin, R. B. Capaz, J. Kim, S. Aloni, W. Wang, X. Bai, S. G. Louie, E. Wang, and F. Wang, Proc. Natl. Acad. Sci. USA **111**, 7564 (2014).

[18] E. Malic and A. Knorr, *Graphene and Carbon Nanotubes: Ultrafast Optics and Relaxation Dynamics* (Wiley-VCH, Weinheim, 2013).

[19] E. Malic, M. Hirtschulz, F. Milde, A. Knorr, and S. Reich, Phys. Rev. B **74**, 195431 (2006).

[20] E. Malic, J. Maultzsch, S. Reich, and A. Knorr, Phys. Rev. B **82**, 035433 (2010).

[21] J. Jiang, R. Saito, G. G. Samsonidze, A. Jorio, S. G. Chou, G. Dresselhaus, and M. S. Dresselhaus, Phys. Rev. B **75**, 035407 (2007).

[22] The effect of external dielectric screening would lead to a slight decrease in this value of the order of 10% to 15%. However, due to the lack of knowledge about the nanoenvironment of the tube in the micelle structure we neglected this contribution.

[23] S. Berger, F. Iglesias, P. Bonnet, C. Voisin, G. Cassabois, J. S. Lauret, C. Delalande, and P. Roussignol, J. Appl. Phys. **105**, 094323 (2009).

[24] E. Verdenhalven and E. Malic, J. Phys. Condens. Matter **25**, 245302 (2013).

[25] K. F. Mak, M. Y. Sfeir, Y. Wu, C. H. Lui, J. A. Misewich, and T. F. Heinz, Phys. Rev. Lett. **101**, 196405 (2008).

[26] J. W. Mintmire and C. T. White, Phys. Rev. Lett. **81**, 2506 (1998).

[27] A. Grüneis, R. Saito, G. G. Samsonidze, T. Kimura, M. A. Pimenta, A. Jorio, A. G. Souza Filho, G. Dresselhaus, and M. S. Dresselhaus, Phys. Rev. B **67**, 165402 (2003).